

Pipeline-Invariant Representation Learning for Neuroimaging

Xinhui Li^{1*}

Alex Fedorov^{1*}

Mrinal Mathur¹

Anees Abrol¹

Gregory Kiar²

Sergey Plis¹

Vince Calhoun¹

XINHUILI@GATECH.EDU

AFEDOROV@GATECH.EDU

MMATHUR4@STUDENT.GSU.EDU

AABROL@GSU.EDU

GREGORY.KIAR@CHILDMIND.ORG

SPLIS@GSU.EDU

VCALHOUN@GSU.EDU

¹*The Georgia State University/Georgia Institute of Technology/Emory University Center for Translational Research in Neuroimaging and Data Science (TReNDS), Atlanta, GA, USA*

²*Child Mind Institute, New York, NY, USA*

Abstract

Deep learning has been widely applied in neuroimaging, including predicting brain-phenotype relationships from magnetic resonance imaging (MRI) volumes. MRI data usually requires extensive preprocessing prior to modeling, but variation introduced by different MRI preprocessing pipelines may lead to different scientific findings, even when using the identical data. Motivated by the data-centric perspective, we first evaluate how preprocessing pipeline selection can impact the downstream performance of a supervised learning model. We next propose two pipeline-invariant representation learning methodologies, *MPSL* and *PXL*, to improve consistency in classification performance and to capture similar neural network representations. Using 2000 human subjects from the UK Biobank dataset, we demonstrate that both models present unique advantages, in particular that MPSL can be used to improve out-of-sample generalization to new pipelines, while PXL can be used to improve predictive performance consistency and representational

similarity. These results suggest that our proposed models can be applied to overcome pipeline-related biases, and to improve prediction consistency and robustness in brain-phenotype modeling.

Keywords: MRI, preprocessing pipeline, representation learning

1. Introduction

Deep learning has been widely applied to establish novel brain-phenotype relationships and to advance our understanding of brain disorders, in part because of its effectiveness in learning nonlinear relationships from neuroimaging data (e.g., magnetic resonance imaging; MRI) (Plis et al., 2014; Abrol et al., 2021). MRI data usually requires extensive preprocessing to mitigate data collection artifacts and transform the data to standard spaces for performing statistical analyses and interpretation of results. In the past decade, a growing array of MRI preprocessing pipelines have been developed, but there remains no consensus standard for preprocessing methods. Though these pipelines share basic preprocessing components, the specific implementation at each

* Corresponding authors

step can be different. Recent studies have shown that pipeline-related variation may result in significantly different preprocessed results and may lead to conflicting scientific conclusions, even when using identical raw data (Botvinik-Nezer et al., 2020; Li et al., 2021). When used in the development of deep learning models, these pipeline-specific biases may be amplified if models learn shortcut strategies based on unique non-biological features (Torralba and Efros, 2011; Geirhos et al., 2020). However, there is little work in the literature evaluating how preprocessing pipelines will affect downstream deep learning task performance.

Recently, the machine learning community has emphasized the importance of shifting from *model-centric* to *data-centric* approaches given that data quality plays an essential role in deep learning applications (Ng, 2021). Motivated by this data-centric perspective, we first evaluate how preprocessed data from different pipelines affect the downstream performance of a supervised learning model. To this end, a uni-pipeline supervised learning (UPSL) model is trained, using a dataset preprocessed by each of three pipelines, respectively. We train these models on a challenging combined age and gender classification task from a previous study (Abrol et al., 2021) to investigate how the model performance is sensitive to pipeline-related variation. We then compare models trained across pipelines through 1) within-sample test accuracy, 2) mutual agreement between pipelines, 3) out-of-sample test accuracy from transfer learning and 4) representational similarity of convolutional layers measured by minibatch centered kernel alignment (CKA) (Nguyen et al., 2020). Our results highlight significant pipeline-related variation and poor generalizability in UPSL.

Next, we propose two approaches to overcome pipeline-related variation and achieve pipeline-invariant representation learning.

First, we suggest a multi-pipeline supervised learning (MPSL) model trained on a dataset pairs to take features from both datasets into account. Second, we introduce a pipeline-based contrastive learning (PXL) model which integrates both supervised and contrastive learning paradigms. These approaches were evaluated similarly to the UPSL models, and our findings demonstrate that both techniques have unique strengths. Specifically, MPSL can improve out-of-sample generalization to new pipelines, while PXL can achieve competitive and consistent performance within a pipeline set. Notably, both MPSL and PXL can improve latent representational similarity.

The key contributions of this study include: 1) evaluation of the impact of neuroimaging preprocessing pipelines on deep learning tasks; 2) proposal of novel methodologies to evaluate learning performance including mutual agreement between pipelines, within-sample and out-of-sample test accuracy, and between-pipeline CKA; 3) development of two pipeline-invariant representation learning methodologies, *MPSL* and *PXL*, to capture pipeline-invariant representations in the latent space and overcome pipeline-related variation in prediction tasks, including when applied to out-of-sample pipelines.

2. Methods

2.1. Data Preprocessing

The T1-weighted structural MRI (sMRI) images of 2000 subjects from UK Biobank dataset (Miller et al., 2016; Abrol et al., 2021) were used in this study. Subjects were grouped into 5 age groups (45 – 52, 53 – 59, 60 – 66, 67 – 73, and 74 – 80 years old) and 2 sex groups (male and female), resulting in 10 labels in total. The 2000 subjects were selected to balance the age and sex categories in the dataset. 1800 subjects with balanced labels were randomly selected and

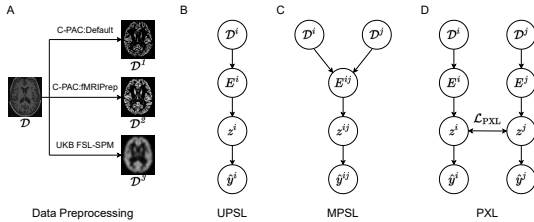


Figure 1: Experiment overview.

then evenly split into 9 folds for hyperparameter optimization and cross-validation. The remaining 200 subjects with balanced labels were used as a hold-out test set. We report the inference performance on the hold-out test set from models trained on 9 folds.

The same sMRI dataset was preprocessed by each of three commonly-used MRI preprocessing pipelines independently: the default pipeline in the Configurable Pipeline for the Analysis of Connectomes (C-PAC:Default) (Craddock et al., 2013), the fMRIPrep-options pipeline in C-PAC (C-PAC:fMRIPrep) (Esteban et al., 2019), and the UK Biobank FSL pipeline followed by SPM (UKB FSL-SPM) (Alfaro-Almagro et al., 2018; Jenkinson et al., 2012; Friston et al., 1994). The detailed preprocessing workflow is described in Appendix A. The preprocessed gray matter volume image, a known biomarker of aging and gender effects (Silva et al., 2021), is used as the input.

2.2. Model Architectures

Uni-Pipeline Supervised Learning To evaluate how data preprocessing affects the prediction result, we trained a supervised learning model in a combined age and gender prediction task for each preprocessed dataset separately, denoted as uni-pipeline supervised learning (UPSL). The UPSL model includes one encoder E^i , taking each of three datasets \mathcal{D}^i as the input, learning representations z^i and predicting labels \hat{y}^i . The encoder network was developed based on

AlexNet (Krizhevsky et al., 2012) because it is widely-used in the neuroimaging literature (Lin et al., 2021; Zhang et al., 2020; Fedorov et al., 2019) and previous work (Abrol et al., 2021) provides a performance benchmark. The AlexNet architecture is described in Appendix B. Each model was then trained for 200 epochs. We repeated the experiment across 9 folds of training and validation data.

Multi-Pipeline Supervised Learning Our first proposed architecture, multi-pipeline supervised learning (MPSL), includes one encoder E^{ij} taking two datasets \mathcal{D}^i and \mathcal{D}^j to learn representations z^{ij} and predict labels \hat{y}^{ij} . The idea of MPSL is to treat pipelines as unique data augmentation transformations. Such strategy doubles the size of training data, but the training process and the model implementation are identical to UPSL.

Pipeline-based Contrastive Learning Our second proposed approach, pipeline-based contrastive learning (PXL), consists of two encoders (E^i, E^j) using the dataset preprocessed by two pipelines ($\mathcal{D}^i, \mathcal{D}^j$) as the inputs separately, and each producing their own sets of output labels (\hat{y}^i and \hat{y}^j). The novel contribution in PXL is to add a contrastive loss term to the supervised loss function to bring the representations from different pipelines closer to each other in the latent space for the same subject, while pushing away the representations for different subjects. The details of the PXL contrastive objective \mathcal{L}_{PXL} are explained in Appendix C and D.

The hyperparameter optimization for each of three models is described in Appendix E.

2.3. Evaluation Metrics

We use three metrics to measure pipeline-invariant learning performance: within-sample inference, mutual agreement across pipelines, and out-of-sample inference. The

within-sample test accuracy was obtained by applying the trained model on the hold-out test set preprocessed by the same pipeline. The mutual agreement across pipelines was calculated as the percentage of overlap between the predicted labels from a pipeline pair \hat{y}^i, \hat{y}^j and the ground truth labels y (i.e. $\hat{y}^i = \hat{y}^j = y$). To evaluate out-of-sample generalizability, we trained a logistic regression model from *scikit-learn* (Pedregosa et al., 2011) using the training set from a different pipeline. The pretrained encoder with fixed parameters served as a feature extractor and the learned representations were preserved during transfer learning. Minibatch CKA is used to measure representational similarity between pipeline pairs (see Appendix F).

3. Results

3.1. PXL achieves competitive within-sample performance while MPSL demonstrates robust out-of-sample generalization.

The UPLS average test accuracy ranges from 0.390 to 0.482, with a difference of 0.092 (Table 1¹ and Figure 2²). The statistical analysis reveals that the test result from UKB FSL-SPM is significantly different from the results from C-PAC:Default and C-PAC:fMRIPrep ($p < 0.05/3$, Wilcoxon signed-rank test, Bonferroni correction). The performance difference between the C-PAC:Default and C-PAC:fMRIPrep pipelines is not significant. We further replicated the UPLS experiment using the DCGAN encoder (Radford et al., 2015), an effective unsupervised representa-

1. MPSL and PXL training set pair order follows Figure 2.
2. Default, fMRIPrep and UKB stand for C-PAC:Default, C-PAC:fMRIPrep and UKB FSL-SPM, respectively. Default (fMRIPrep) indicates test performance on Default when trained with Default and fMRIPrep together.

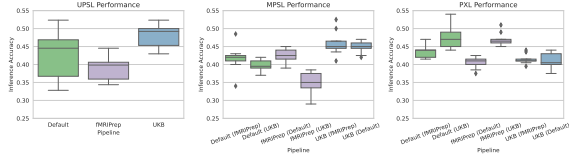


Figure 2: Within-sample test performance.

Table 1: Within-sample test performance.

Model	Default	fMRIPrep	UKB
UKB	0.420 ± 0.064	0.390 ± 0.032	0.482 ± 0.030
MPSL	0.416 ± 0.035	0.424 ± 0.018	0.460 ± 0.032
	0.398 ± 0.015	0.347 ± 0.033	0.448 ± 0.016
PXL	0.437 ± 0.019	0.406 ± 0.016	0.415 ± 0.013
	0.474 ± 0.030	0.469 ± 0.018	0.407 ± 0.022

tion learning encoder, and observed a similar inference difference of 0.069 across pipelines (see Appendix G). The UPLS result indicates that preprocessed data from different pipelines will significantly affect the downstream performance.

In MPSL, the overall performance is more consistent, except that the C-PAC:fMRIPrep test set result from the C-PAC:fMRIPrep and UKB FSL-SPM training set pair is lower than the others. The MPSL result shows that pipeline-related variation can be mitigated by incorporating multiple preprocessed datasets during training. In PXL, the performance difference 0.068 is the smallest among three models, with smaller cross-fold variance observed. Interestingly, the inference performance on the C-PAC:Default and C-PAC:fMRIPrep test sets becomes significantly better when the encoder utilizes the UKB FSL-SPM dataset during training, though the inference performance on the UKB FSL-SPM test set slightly drops compared to UPLS and MPSL. Both MPSL and PXL demonstrate higher mutual agreement than UPLS (Table 2). Specifically, PXL shows the best performance in C-PAC:fMRIPrep and UKB FSL-SPM pair while MPSL is the best in the other pairs.

The out-of-sample transfer learning performance, which measures model generaliz-

Table 2: Mutual agreement.

Model	Default fMRIPrep	Default UKB	fMRIPrep UKB
UKB	0.206 ± 0.030	0.228 ± 0.043	0.228 ± 0.014
MPSL	0.233 ± 0.028	0.259 ± 0.022	0.228 ± 0.017
PXL	0.217 ± 0.016	0.226 ± 0.028	0.246 ± 0.015

Table 3: Out-of-sample transfer learning inference performance.

Model	Default	fMRIPrep	UKB
UKB	-	0.273 ± 0.029	0.263 ± 0.020
	0.302 ± 0.027	-	0.277 ± 0.023
	0.223 ± 0.030	0.247 ± 0.021	-
MPSL	0.297 ± 0.018	0.280 ± 0.011	0.292 ± 0.020
PXL	0.231 ± 0.080	0.261 ± 0.091	0.237 ± 0.097
	0.157 ± 0.062	0.184 ± 0.063	0.219 ± 0.075

ability, is presented in Table 3³. We observe the best generalization performance from MPSL models (average across all models of 0.290), as well as fairly good performance from the UPSL models (average across all models of 0.264). However, PXL performance is not superior when transferred to an unseen test set, suggesting the learned features are not guaranteed to generalize across pipeline populations.

3.2. MPSL and PXL capture more similar between-pipeline representations to UPSL.

As shown in Figure 3, between-pipeline representations from the last three layers are more similar while those from the first three layers are less similar. Both MPSL and PXL have higher CKA values than UPSL, suggesting the learned representations from MPSL and PXL are more similar than UPSL. Among three models, PXL has the highest average between-pipeline CKA value 0.718

3. Each row in UPSL is from Default, fMRIPrep and UKB training set, respectively. Each column in MPSL and PXL is from fMRIPrep - UKB, Default - UKB, and Default - fMRIPrep training set pair, respectively.

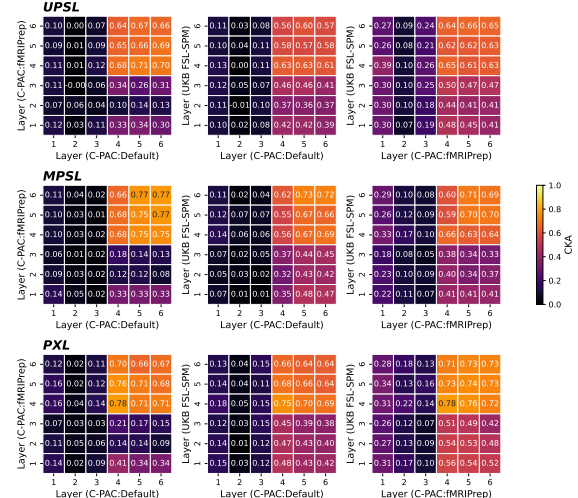


Figure 3: Between-pipeline CKA.

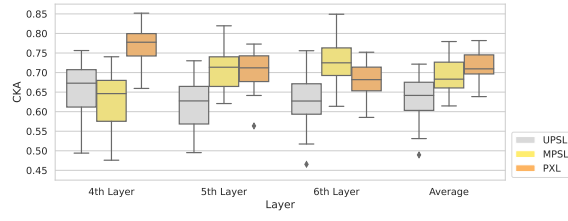


Figure 4: Between-pipeline CKA in the last three layers.

across the last three layers (see Appendix H Table H.1). Figure 4 also demonstrates that highly similar between-pipeline representations learned by MPSL and PXL in the last three layers. Further, we performed experiments on natural image datasets and showed that PXL can improve representational similarity compared to UPSL (see Appendix I).

4. Discussion

The contributions of the present work are two-fold. First, we evaluated the impact of neuroimaging preprocessing pipelines and preprocessed data quality in deep learning tasks, and demonstrated current limitations

of UPSL. The UPSL result demonstrates that the same dataset preprocessed by different pipelines can result in significantly different prediction performance. As shown in Figure 2, the average test accuracy difference from UPSL can be as high as 9.2% when using datasets preprocessed by different pipelines. The result emphasizes the importance of clear scientific communication surrounding decisions in neuroimaging preprocessing, and making pipelines publicly available to allow for evaluation, comparison, and reproduction in the context of downstream learning tasks.

Next, we proposed two approaches, MPSL and PXL, to overcome pipeline-related variation. While the MPSL approach is a naive extension of UPSL, we noted that the MPSL approach led to consistent within-sample performance while also improving out-of-sample generalizability. We hypothesize this is because the MPSL model was less prone to learning pipeline-specific features, and pipeline differences forced the optimization to identify features that discriminated participants across more biologically-meaningful features. Our novel approach PXL adopts a contrastive loss function leading to the improved within-sample performance. Specifically, PXL achieved the highest within-sample test accuracy on the C-PAC:Default and C-PAC:fMRIPrep datasets, though the UKB FSL-SPM performance dropped relative to UPSL and MPSL (Table 1). One possibility is that the contrastive objective in PXL learns the shared information from both views and may tend to capture high-frequency texturized features but not low-frequency information from UKB FSL-SPM, the only pipeline which applies spatial smoothing. UKB FSL-SPM smoothed out texturized information that includes individual variability and thus achieved the best within-sample test performance in UPSL. We note that PXL shows relatively poor out-

of-sample performance. Previous study also reports that the objective leading to better performance at the original task may fail at transfer tasks (Kornblith et al., 2021). Notably, both MPSL and PXL capture more similar representations in the last three layers (Figure 4), supporting their potentials to achieve pipeline-invariant learning.

Future work will evaluate these approaches on other neuroimaging modalities such as functional MRI that incorporates temporal dynamics as well as on a wider range of tasks including brain disorder prediction. We will also investigate the possibility to design a more generalizable model which can perform well on both within-sample and out-of-sample datasets. Furthermore, MPSL and PXL can be applied to mitigate site effects or data acquisition effects. The experiments on natural image datasets (Appendix I) support the feasibility of pairing samples by labels in the contrastive learning paradigm.

In summary, we demonstrated the pipeline-related variation can make a significant difference in the prediction result of a downstream task. We then proposed two pipeline-invariant representation learning approaches, MPSL and PXL, to mitigate the bias introduced by data preprocessing. Our results demonstrated that MPSL and PXL can achieve robust and consistent within-sample and out-of-sample inference performance and improve representational similarity in the latent space. The proposed models can be applied to mitigate pipeline-related variation and improve prediction consistency and robustness in brain-phenotype modeling.

Acknowledgments

This work was supported by NSF grant #2112455 and NIH grant R01MH118695.

References

Anees Abrol, Zening Fu, Mustafa Salman, Rogers Silva, Yuhui Du, Sergey Plis, and Vince Calhoun. Deep learning encodes robust discriminative neuroimaging representations to outperform standard machine learning. *Nature Communications*, 12:353, 2021. doi: 10.1038/s41467-020-20655-6.

Fidel Alfaro-Almagro, Mark Jenkinson, Neal K Bangerter, Jesper LR Andersson, Ludovica Griffanti, Gwenaëlle Douaud, Stamatios N Sotiropoulos, Saad Jbabdi, Moises Hernandez-Fernandez, Emmanuel Vallee, et al. Image processing and quality control for the first 10,000 brain imaging datasets from uk biobank. *Neuroimage*, 166:400–424, 2018.

Jesper LR Andersson, Mark Jenkinson, and Stephen Smith. Non-linear optimisation fmrib technical report tr07ja1. *Practice*, 2007a.

Jesper LR Andersson, Mark Jenkinson, Stephen Smith, et al. Non-linear registration, aka spatial normalisation fmrib technical report tr07ja2. *FMRIB Analysis Group of the University of Oxford*, 2 (1):e21, 2007b.

Brian B Avants, Charles L Epstein, Murray Grossman, and James C Gee. Symmetric diffeomorphic image registration with cross-correlation: evaluating automated labeling of elderly and neurodegenerative brain. *Medical image analysis*, 12(1):26–41, 2008.

Philip Bachman, R Devon Hjelm, and William Buchwalter. Learning representations by maximizing mutual information across views. *Advances in neural information processing systems*, 32, 2019.

Rotem Botvinik-Nezer et al. Variability in the analysis of a single neuroimaging dataset by many teams. *Nature*, 2020. doi: 10.1038/s41586-020-2314-9.

Ting Chen, Simon Kornblith, Mohammad Norouzi, and Geoffrey E. Hinton. A simple framework for contrastive learning of visual representations. *CoRR*, abs/2002.05709, 2020.

Sumit Chopra, Raia Hadsell, and Yann LeCun. Learning a similarity metric discriminatively, with application to face verification. In *2005 IEEE Computer Society Conference on Computer Vision and Pattern Recognition (CVPR'05)*, volume 1, pages 539–546. IEEE, 2005.

Robert W Cox. Afni: software for analysis and visualization of functional magnetic resonance neuroimages. *Computers and Biomedical research*, 29(3):162–173, 1996.

Cameron Craddock, Sharad Sikka, Brian Cheung, Ranjeet Khanuja, Satrajit S Ghosh, Chaogan Yan, Qingyang Li, Daniel Lurie, Joshua Vogelstein, Randal Burns, et al. Towards automated analysis of connectomes: The configurable pipeline for the analysis of connectomes (c-pac). *Front Neuroinform*, 42:10–3389, 2013.

Oscar Esteban, Christopher J Markiewicz, Ross W Blair, Craig A Moodie, A Ilkay Isik, Asier Erramuzpe, James D Kent, Mathias Goncalves, Elizabeth DuPre, Madeleine Snyder, Hiroyuki Oya, Satrajit S Ghosh, Jessey Wright, Joke Durnez, Russell A Poldrack, and Krzysztof J Gorgolewski. fmriprep: a robust preprocessing pipeline for functional mri. *Nature methods*, 16(1):111–116, 2019.

Alex Fedorov, R Devon Hjelm, Anees Abrol, Zening Fu, Yuhui Du, Sergey Plis, and

Vince D Calhoun. Prediction of progression to alzheimer’s disease with deep informax. In *2019 IEEE EMBS International conference on biomedical & health informatics (BHI)*, pages 1–5. IEEE, 2019.

Karl J Friston, Andrew P Holmes, Keith J Worsley, J-P Poline, Chris D Frith, and Richard SJ Frackowiak. Statistical parametric maps in functional imaging: a general linear approach. *Human brain mapping*, 2(4):189–210, 1994.

Robert Geirhos, Jörn-Henrik Jacobsen, Claudio Michaelis, Richard Zemel, Wieland Brendel, Matthias Bethge, and Felix A. Wichmann. Shortcut learning in deep neural networks. *Nature Machine Intelligence*, 2(11):665–673, nov 2020. doi: 10.1038/s42256-020-00257-z.

Günther Grabner, Andrew L Janke, Marc M Budge, David Smith, Jens Pruessner, and D Louis Collins. Symmetric atlasing and model based segmentation: an application to the hippocampus in older adults. In *International Conference on Medical Image Computing and Computer-Assisted Intervention*, pages 58–66. Springer, 2006.

Arthur Gretton, Olivier Bousquet, Alex Smola, and Bernhard Schölkopf. Measuring statistical dependence with hilbert-schmidt norms. In *International conference on algorithmic learning theory*, pages 63–77. Springer, 2005.

Michael Gutmann and Aapo Hyvärinen. Noise-contrastive estimation: A new estimation principle for unnormalized statistical models. In Yee Whye Teh and Mike Titterington, editors, *Proceedings of the Thirteenth International Conference on Artificial Intelligence and Statistics*, volume 9 of *Proceedings of Machine Learning Research*, pages 297–304, Chia Laguna Resort, Sardinia, Italy, 13–15 May 2010. PMLR.

Raia Hadsell, Sumit Chopra, and Yann LeCun. Dimensionality reduction by learning an invariant mapping. In *2006 IEEE Computer Society Conference on Computer Vision and Pattern Recognition (CVPR’06)*, volume 2, pages 1735–1742. IEEE, 2006.

David R Hardoon, Sandor Szegedy, and John Shawe-Taylor. Canonical correlation analysis: An overview with application to learning methods. *Neural computation*, 16(12):2639–2664, 2004.

Dan Hendrycks, Mantas Mazeika, Saurav Kadavath, and Dawn Song. Using self-supervised learning can improve model robustness and uncertainty. *Advances in Neural Information Processing Systems*, 32, 2019.

R Devon Hjelm, Alex Fedorov, Samuel Lavoie-Marchildon, Karan Grewal, Phil Bachman, Adam Trischler, and Yoshua Bengio. Learning deep representations by mutual information estimation and maximization. *arXiv preprint arXiv:1808.06670*, 2018.

Mark Jenkinson and Stephen Smith. A global optimisation method for robust affine registration of brain images. *Medical image analysis*, 5(2):143–156, 2001.

Mark Jenkinson, Peter Bannister, Michael Brady, and Stephen Smith. Improved optimization for the robust and accurate linear registration and motion correction of brain images. *Neuroimage*, 17(2):825–841, 2002.

Mark Jenkinson, Christian F Beckmann, Timothy EJ Behrens, Mark W Woolrich, and Stephen M Smith. Fsl. *Neuroimage*, 62(2):782–790, 2012.

Diederik P Kingma and Jimmy Ba. Adam: A method for stochastic optimization. *arXiv preprint arXiv:1412.6980*, 2014.

Simon Kornblith, Mohammad Norouzi, Honglak Lee, and Geoffrey Hinton. Similarity of neural network representations revisited. In *International Conference on Machine Learning*, pages 3519–3529. PMLR, 2019.

Simon Kornblith, Ting Chen, Honglak Lee, and Mohammad Norouzi. Why do better loss functions lead to less transferable features? *Advances in Neural Information Processing Systems*, 34, 2021.

Alex Krizhevsky, Ilya Sutskever, and Geoffrey E Hinton. Imagenet classification with deep convolutional neural networks. In F. Pereira, C. J. C. Burges, L. Bottou, and K. Q. Weinberger, editors, *Advances in Neural Information Processing Systems*, volume 25. Curran Associates, Inc., 2012.

Yann LeCun, Léon Bottou, Yoshua Bengio, and Patrick Haffner. Gradient-based learning applied to document recognition. *Proceedings of the IEEE*, 86(11):2278–2324, 1998.

Xinhui Li, Lei Ai, Steve Giavasis, Hecheng Jin, Eric Feczkó, Ting Xu, Jon Clucas, Alexandre Franco, Anibal Sólon Heinsfeld, Azeez Adebimpe, Joshua Vogelstein, Chao-Gan Yan, Oscar Esteban, Russell Poldrack, Cameron Craddock, Damien Fair, Theodore Satterthwaite, Gregory Kiar, and Michael Milham. Moving beyond processing and analysis-related variation in neuroscience. *bioRxiv*, 2021. doi: 10.1101/2021.12.01.470790.

Lan Lin, Ge Zhang, Jingxuan Wang, Miao Tian, and Shuicai Wu. Utilizing transfer learning of pre-trained alexnet and relevance vector machine for regression for predicting healthy older adult’s brain age from structural mri. *Multimedia Tools and Applications*, 80(16):24719–24735, 2021.

Liyuan Liu, Haoming Jiang, Pengcheng He, Weizhu Chen, Xiaodong Liu, Jianfeng Gao, and Jiawei Han. On the variance of the adaptive learning rate and beyond. *arXiv preprint arXiv:1908.03265*, 2019.

Karla L Miller, Fidel Alfaro-Almagro, Neal K Bangerter, David L Thomas, Essa Yacoub, Junqian Xu, Andreas J Bartsch, Saad Jbabdi, Stamatis N Sotropoulos, Jesper LR Andersson, et al. Multi-modal population brain imaging in the uk biobank prospective epidemiological study. *Nature neuroscience*, 19(11):1523–1536, 2016.

Ari Morcos, Maithra Raghu, and Samy Bengio. Insights on representational similarity in neural networks with canonical correlation. *Advances in Neural Information Processing Systems*, 31, 2018.

Yuval Netzer, Tao Wang, Adam Coates, Alessandro Bissacco, Bo Wu, and Andrew Y Ng. Reading digits in natural images with unsupervised feature learning. *NIPS Workshop on Deep Learning and Unsupervised Feature Learning*, 2011.

Andrew Ng. Mlops: From model-centric to data-centric ai, 2021.

Thao Nguyen, Maithra Raghu, and Simon Kornblith. Do wide and deep networks learn the same things? uncovering how neural network representations vary with width and depth. *arXiv preprint arXiv:2010.15327*, 2020.

F. Pedregosa, G. Varoquaux, A. Gramfort, V. Michel, B. Thirion, O. Grisel, M. Blondel, P. Prettenhofer, R. Weiss, V. Dubourg, J. Vanderplas, A. Passos, D. Cournapeau, M. Brucher, M. Perrot,

and E. Duchesnay. Scikit-learn: Machine learning in Python. *Journal of Machine Learning Research*, 12:2825–2830, 2011.

Sergey M Plis, Devon R Hjelm, Ruslan Salakhutdinov, Elena A Allen, Henry J Bockholt, Jeffrey D Long, Hans J Johnson, Jane S Paulsen, Jessica A Turner, and Vince D Calhoun. Deep learning for neuroimaging: a validation study. *Frontiers in neuroscience*, 8:229, 2014.

Alec Radford, Luke Metz, and Soumith Chintala. Unsupervised representation learning with deep convolutional generative adversarial networks. *arXiv preprint arXiv:1511.06434*, 2015.

Maithra Raghu, Justin Gilmer, Jason Yosinski, and Jascha Sohl-Dickstein. Svcca: Singular vector canonical correlation analysis for deep learning dynamics and interpretability. *Advances in neural information processing systems*, 30, 2017.

Rogers F Silva, Eswar Damaraju, Xinhui Li, Peter Kochonov, Aysenil Belger, Judith M Ford, Sarah McEwen, Daniel H Mathalon, Bryon A Mueller, Steven G Potkin, et al. Multimodal iva fusion for detection of linked neuroimaging biomarkers. *bioRxiv*, 2021.

Stephen M Smith. Fast robust automated brain extraction. *Human brain mapping*, 17(3):143–155, 2002.

Le Song, Alex Smola, Arthur Gretton, Justin Bedo, and Karsten Borgwardt. Feature selection via dependence maximization. *Journal of Machine Learning Research*, 13 (5), 2012.

Antonio Torralba and Alexei A. Efros. Unbiased look at dataset bias. In *CVPR 2011*, pages 1521–1528, 2011. doi: 10.1109/CVPR.2011.5995347.

Nicholas J Tustison, Brian B Avants, Philip A Cook, Yuanjie Zheng, Alexander Egan, Paul A Yushkevich, and James C Gee. N4itk: improved n3 bias correction. *IEEE transactions on medical imaging*, 29 (6):1310–1320, 2010.

Aaron Van den Oord, Yazhe Li, and Oriol Vinyals. Representation learning with contrastive predictive coding. *arXiv e-prints*, pages arXiv–1807, 2018.

Zhirong Wu, Yuanjun Xiong, Stella X Yu, and Dahua Lin. Unsupervised feature learning via non-parametric instance discrimination. In *Proceedings of the IEEE conference on computer vision and pattern recognition*, pages 3733–3742, 2018.

Jianing Zhang, Xuechen Li, Yuexiang Li, Mingyu Wang, Bingsheng Huang, Shuqiao Yao, and Linlin Shen. Three dimensional convolutional neural network-based classification of conduct disorder with structural mri. *Brain imaging and behavior*, 14(6):2333–2340, 2020.

Yongyue Zhang, Michael Brady, and Stephen Smith. Segmentation of brain mr images through a hidden markov random field model and the expectation-maximization algorithm. *IEEE transactions on medical imaging*, 20(1):45–57, 2001.

Appendix A. Preprocessing workflows

The detailed preprocessing workflow of each pipeline is as follows: 1) The *C-PAC:Default* structural preprocessing workflow performs brain extraction via AFNI 3dSkullStrip (Cox, 1996), tissue segmentation via FSL FAST (Zhang et al., 2001), and spatial normalization via ANTs SyN non-linear alignment (Avants et al., 2008). 2) The *C-PAC:fMRIPrep* structural pipeline

applies ANTs N4 bias field correction (Tustison et al., 2010) on the raw images, followed by ANTs brain extraction, a custom thresholding and erosion algorithm to generate tissue segmentation masks (Esteban et al., 2019), and ANTs SyN alignment to transform the data to the standard space. ANTs registration is performed using skull-stripped images, unlike the C-PAC:Default pipeline which uses whole-head images. 3) The *UKB FSL-SPM* pipeline runs a gradient distortion correction and calculates linear and non-linear transformations via FSL FLIRT (Jenkinson and Smith, 2001; Jenkinson et al., 2002) and FNIRT (Andersson et al., 2007a,b), respectively. Then it performs brain extraction via FSL BET (Smith, 2002) and segments the sMRI data into tissue probability maps. The gray matter images are then warped to standard space, modulated and smoothed using a Gaussian kernel with an FWHM = 10 mm using SPM12 (Friston et al., 1994).

All preprocessed gray matter volume images are in MNI (2006) space (Grabner et al., 2006). The dimensions of the gray matter volume image are $91 \times 109 \times 91$, corresponding to a voxel size of $2 \times 2 \times 2 \text{ mm}^3$.

Appendix B. AlexNet architecture

The AlexNet encoder includes 5 convolutional layers and 1 average pooling layer. The 5 convolutional layers have 64, 128, 192, 192, 64 output units, and $62^3, 18^3, 6^3, 6^3$ output dimensions, respectively. The last convolutional layer with 64 output units defines a 64 dimensional representation.

Appendix C. Contrastive loss in PXL

We hypothesize that preprocessing pipelines may introduce unintended biases to the dataset and thus result in disagreement of

learned representations and model performance. To mitigate pipeline-related biases, we aim to learn pipeline-invariant representations by maximizing agreement between differently preprocessed views of data.

The goal of contrastive representation learning is to learn a latent space where representations of similar sample pairs are closer while representations of dissimilar ones are further apart. The PXL architecture is inspired by recent work on contrastive learning. Early applications of contrastive loss can be traced back to learning invariant mappings of certain input transformations (Chopra et al., 2005; Hadsell et al., 2006). Several recent advances are rooted in Noise Contrastive Estimation (NCE) (Gutmann and Hyvärinen, 2010) including Memory Bank (Wu et al., 2018), Contrastive Predictive Coding (Van den Oord et al., 2018) and Deep InfoMax (Hjelm et al., 2018). More recently, SimCLR (Chen et al., 2020) was proposed to train an encoder network and a projection head to maximize agreement between different views of the identical data via a contrastive loss. Moreover, self-supervision can improve model robustness when combining with a supervised loss (Hendrycks et al., 2019). PXL is developed by adding a contrastive loss to the supervised loss. The contrastive loss, defined by the NCE lower bound, is trained to bring representations from the same subject closer while pushing away those from different subjects in the latent space. Thus, PXL aims to learn pipeline-invariant latent representations.

The details of the contrastive objective in PXL are explained as below. Let $\mathcal{D} = \{(x^i, x^j; y) \sim (\mathcal{D}^i, \mathcal{D}^j)\}$ be a dataset of paired samples $(x^i, x^j; y)$, where x^i is an input image from one dataset \mathcal{D}^i , x^j is an input image from another dataset \mathcal{D}^j , and y is a class label. Then we learn two independent encoders E^i and E^j parameterized by convolutional neural networks that map input images x^i

and x^j to representations $z^i = E^i(x^i)$ and $z^j = E^j(x^j)$. To learn the parameters of the encoders, we optimize the PXL objective:

$$\mathcal{L}_{\text{PXL}} = \lambda \cdot \ell_{\text{supervised}} + (1 - \lambda) \cdot \ell_{\text{contrastive}}, \quad (1)$$

where λ is trade-off hyperparameter between the supervised and contrastive loss. Note that the approach can become self-supervision when $\lambda = 0$ and it can also turn to a fully supervised model by setting $\lambda = 1$, equivalent to MPSL with two encoders. We evaluate how the choice of λ affects model performance and representational similarity in Appendix D. The supervised loss $\ell_{\text{supervised}}$ is defined as sum of cross-entropy losses ℓ_{CE} for pipeline i and j :

$$\ell_{\text{supervised}} = \ell_{\text{CE}}(g^i(z^i); y) + \ell_{\text{CE}}(g^j(z^j); y), \quad (2)$$

where g is a linear projection head from representations to class labels. The contrastive loss term $\ell_{\text{contrastive}}$ follows the Noise Contrastive Estimation (NCE) lower bound definition by (Gutmann and Hyvärinen, 2010). For the n -th sample with a positive pair (z_n^i, z_n^j) , the contrastive objective from pipeline i to pipeline j is:

$$\ell_{i \rightarrow j}(z_n^i, z_n^j) = -\log \frac{e^{f(h_n^i, h_n^j)}}{\sum_{m=1}^N \mathbb{1}_{[m \neq n]} e^{f(h_n^i, h_m^j)}}, \quad (3)$$

where N is the total number of training subjects, f is a critic function and h^i is a projection head for pipeline i , $h_n^i = h^i(z_n^i)$ (Chen et al., 2020). For the choice of critic f , we use scaled dot product and proposed regularization techniques as L_2 penalty and soft hyperbolic tangent (\tanh) clipping of the critic scores (Bachman et al., 2019). The contrastive loss is calculated in both directions to ensure its symmetry.

The final contrastive objective is defined as:

$$\ell_{\text{contrastive}} = \ell_{i \rightarrow j} + \ell_{j \rightarrow i}. \quad (4)$$

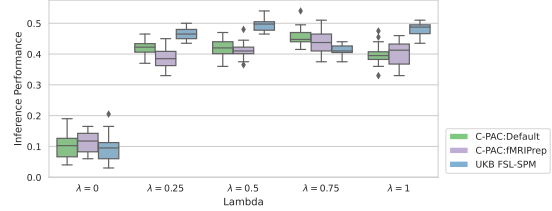


Figure D.1: **Within-sample inference performance for different trade-off parameters λ in the contrastive objective.** The box plot shows the within-sample test accuracy across 3 models from 9 cross-validation derived folds.

Appendix D. Evaluation of the trade-off parameter in the PXL objective

We vary the trade-off parameter λ between the supervised and contrastive loss in the PXL objective \mathcal{L}_{PXL} ($\lambda = 0, 0.25, 0.5, 0.75, 1$) and evaluate how λ affects the model performance and the representational similarity.

As shown in Figure D.1 and Table D.1, we note that the inference performance is better when a larger λ value is applied. Note that there is no classification head being trained when $\lambda = 0$, which explains why the performance is relatively poor. The performance slightly improves when λ increases from 0.25 to 1, implying that the supervised loss plays a more important role in improving the inference performance.

According to Figure D.2, we observe that CKA values in the last three layers are negatively correlated with the λ value, suggesting that the contrastive loss is the key to improve between-pipeline representational similarity.

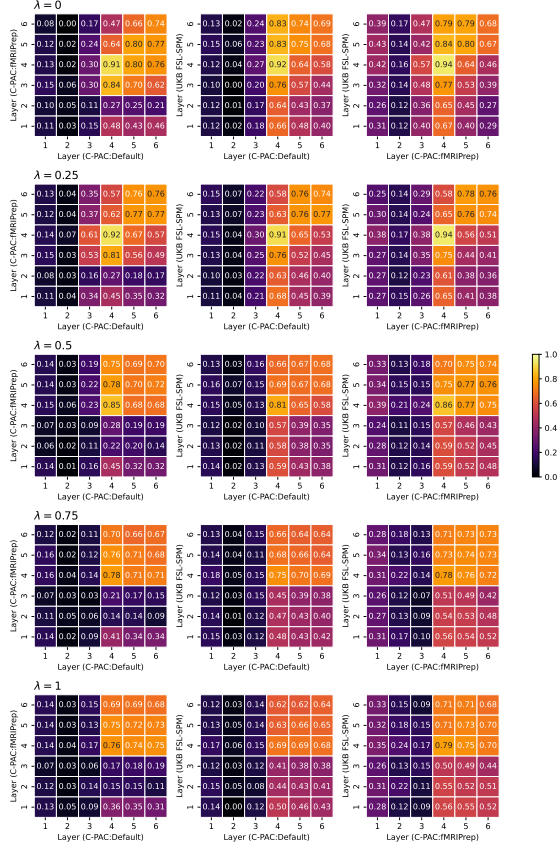


Figure D.2: **PXL between-pipeline CKA across layers.** The average CKA across models from 9 folds shows the last three layers share more similar representations in the hold-out test set. When λ is smaller, the contrastive loss takes a larger percentage of the PXL objective, leading to more similar representations in the last three layers.

Table D.1: **Out-of-sample transfer learning inference performance for different trade-off parameters λ in the contrastive objective.** Each column is evaluated at the training set pair C-PAC:fMRIPrep - UKB FSL-SPM, C-PAC:Default - UKB FSL-SPM, and C-PAC:Default - C-PAC:fMRIPrep, respectively.

λ	Default	fMRIPrep	UKB
0	0.178 ± 0.087 0.165 ± 0.036	0.196 ± 0.071 0.186 ± 0.063	0.188 ± 0.066 0.172 ± 0.081
0.25	0.237 ± 0.126 0.134 ± 0.039	0.260 ± 0.070 0.202 ± 0.062	0.261 ± 0.065 0.207 ± 0.097
0.5	0.175 ± 0.072 0.154 ± 0.049	0.212 ± 0.103 0.179 ± 0.054	0.263 ± 0.089 0.169 ± 0.077
0.75	0.231 ± 0.080 0.157 ± 0.062	0.261 ± 0.091 0.184 ± 0.063	0.237 ± 0.097 0.219 ± 0.075
1	0.191 ± 0.086 0.231 ± 0.055	0.202 ± 0.094 0.164 ± 0.059	0.228 ± 0.116 0.124 ± 0.049

Appendix E. Hyperparameter search

All models were implemented on the PyTorch framework and trained with NVIDIA V100 GPUs.

UPSL We performed hyperparameter tuning by varying batch size (2, 4, 8, 16, 32, 64) and learning rate (10^{-2} , 10^{-3} , 10^{-4} , 10^{-5}) options, and we selected batch size 4 and learning rate 10^{-3} according to the validation performance.

MPSL We performed the same hyperparameter search as UPSL, and selected batch size 32 and learning rate 10^{-3} for MPSL.

PXL Apart from batch size and learning rate, we performed hyperparameter search over identity projection, linear projection and projection with 1, 2 or 3 hidden layers with dimensionality identical to the representation to choose the projection head h . We evaluated five trade-off parameters (0, 0.25, 0.5, 0.75, 1) to balance the supervised loss

and the contrastive loss. We also compared the Adam optimizer (Kingma and Ba, 2014) and the RAdam optimizer (Liu et al., 2019).

After hyperparameter search, we used an identity projection head, batch size 4, learning rate 10^{-4} , trade-off parameter λ 0.75 and the Adam optimizer in the PXL model.

Appendix F. Minibatch centered kernel alignment

To understand neural network representations, recent studies have proposed various methods including canonical correlation analysis (CCA) (Hardoon et al., 2004), singular vector canonical correlation analysis (SVCCA) (Raghu et al., 2017), projection-weighted CCA (PWCCA) (Morcos et al., 2018) and centered kernel alignment (CKA) (Kornblith et al., 2019). Among all approaches, CKA can reliably measure similarities of representations whose dimensions are higher than the number of samples, and consistently identify correspondences between layers across different neural network architectures and initializations (Kornblith et al., 2019). We utilized minibatch CKA (Nguyen et al., 2020) to evaluate representational similarity because of its computational efficiency for high-dimensional neuroimaging data.

The mechanism of minibatch CKA is described as follows. Let $\mathbf{X} \in \mathbb{R}^{m \times u_1}$ and $\mathbf{Y} \in \mathbb{R}^{m \times u_2}$ denote representations of two layers, where m is the number of samples, and u_1 and u_2 are the number of neuron units in \mathbf{X} and \mathbf{Y} , respectively. Here, m is 200 subjects in the test set. We flattened channels c and three spatial dimensions (width w , height h , depth d) of a convolutional layer into u neurons to compare representations of different layers, i.e. $u = c \times h \times w \times d$ (Raghu et al., 2017). We then randomly split m subjects into k minibatches and each minibatch contains n subjects. Let $\mathbf{X}_i \in \mathbb{R}^{n \times u_1}$ and $\mathbf{Y}_i \in \mathbb{R}^{n \times u_2}$ denote representations of

two layers in the i th batch. We then compute the similarity matrices $\mathbf{K} = \mathbf{X}_i \mathbf{X}_i^T$ and $\mathbf{L} = \mathbf{Y}_i \mathbf{Y}_i^T$ and estimate the similarity of the similarity matrices using Hilbert-Schmidt Independence Criterion (HSIC) (Gretton et al., 2005).

Minibatch CKA is computed by averaging the linear CKA across k minibatches:

$$\text{CKA} = \frac{\frac{1}{k} \sum_{i=1}^k \text{H}(\mathbf{K}, \mathbf{L})}{\sqrt{\frac{1}{k} \sum_{i=1}^k \text{H}(\mathbf{K}, \mathbf{K})} \sqrt{\frac{1}{k} \sum_{i=1}^k \text{H}(\mathbf{L}, \mathbf{L})}}, \quad (5)$$

An unbiased estimator of HSIC (Song et al., 2012) is used in minibatch CKA:

$$\text{H}(\mathbf{K}, \mathbf{L}) = \frac{1}{n(n-3)} (\text{tr}(\tilde{\mathbf{K}}\tilde{\mathbf{L}}) + \frac{\mathbf{1}^T \tilde{\mathbf{K}} \mathbf{1} \mathbf{1}^T \tilde{\mathbf{L}} \mathbf{1}}{(n-1)(n-2)} - \frac{2}{n-2} \mathbf{1}^T \tilde{\mathbf{K}} \tilde{\mathbf{L}} \mathbf{1}), \quad (6)$$

where $\tilde{\mathbf{K}}$ and $\tilde{\mathbf{L}}$ are obtained by setting the diagonal entries of \mathbf{K} and \mathbf{L} to zero.

We include 8 subjects in each minibatch in our study. Note that the CKA values are independent of the selection of batch sizes because of the unbiased estimator of HSIC. Detailed proof of the feasibility of using minibatch CKA to approximate CKA can be found in (Nguyen et al., 2020).

Appendix G. Experiments using the DCGAN encoder

To further verify the pipeline effect in a different encoder, we replicated the UPSL experiment using an effective unsupervised representation learning encoder – deep convolutional generative adversarial network (DCGAN) (Radford et al., 2015). We observed a similar pipeline-related effect – the average within-sample inference accuracies across 9 folds are 35.67%, 37.61%, 42.61% for C-PAC: Default, C-PAC: fMRIPrep and UKB FSL-SPM, respectively (Figure G.1). The result on the DCGAN encoder demonstrates that the pipeline-related variability exists across different encoders.

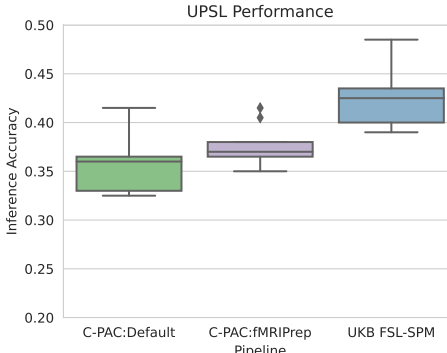


Figure G.1: **UPSL within-sample inference performance using the DCGAN encoder.**

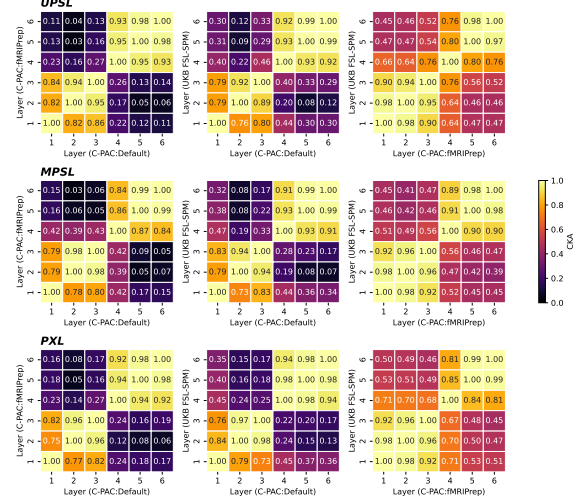


Figure H.1: **Cross-layer within-pipeline CKA.**

Table H.1: **Between-pipeline CKA.**

Model	UPSL	MPSL	PXL
4th Layer	0.652 ± 0.071	0.632 ± 0.069	0.771 ± 0.043
5th Layer	0.619 ± 0.066	0.705 ± 0.049	0.705 ± 0.047
6th Layer	0.629 ± 0.065	0.730 ± 0.054	0.679 ± 0.046
Average	0.633 ± 0.059	0.689 ± 0.044	0.718 ± 0.035

Appendix H. CKA results

As shown in Figure H.1, the within-pipeline CKA across six layers illustrates how the neural network learns for each model. We observe that the first three layers are more similar to each other, and the last three layers are more similar, but the similarity between the first three and last three layers are low across all three learning paradigms. Table H.1 presents the mean and the standard deviation of between-pipeline CKA values at the fourth, fifth and sixth layer and the average across these three layers. Among three models, PXL shows the highest average CKA values across the last three layers.

Appendix I. Experiments on natural image datasets

We have demonstrated that PXL can achieve consistent within-sample inference performance and capture similar cross-layer

between-pipeline representations on datasets paired by subjects. To further validate the feasibility of PXL on samples paired by labels, we perform UPSL and PXL experiments on two natural image datasets, two-view MNIST and MNIST-SVHN, in which images are paired by labels. We then measure similarity across layers using minibatch CKA.

I.1. Datasets

Two natural image datasets, two-view MNIST and MNIST-SVHN, are used to validate the feasibility of PXL in a broader context of multi-view and multi-domain learning.

Two-view MNIST The two-view MNIST dataset contains two corrupted views of digits from the MNIST dataset (LeCun et al., 1998). The image preprocessing is as follows. First of all, the intensities of each image are rescaled to a unit interval and then the size of each image is rescaled to 32×32 to fit the DCGAN architecture. In the first view, the image is randomly rotated at an an-

gle uniformly sampled from $[-\frac{\pi}{4}, \frac{\pi}{4}]$. In the second view, we add a noise sampled from a uniform distribution $[0, 1]$ to the image and additionally rescale the image intensities to a unit interval. The cross-validation dataset is generated using stratified 5-fold split from the original training MNIST set, including 48,000 and 12,000 images in the training and validation set, respectively. The original 10,000 MNIST test set is used as the hold-out set.

MNIST-SVHN The MNIST-SVHN dataset includes samples with two views — grayscale MNIST digits as the first view and RGB street view house numbers sampled from the SVHN dataset (Netzer et al., 2011) as the second view. The dataset generation process is almost identical to the description at <https://github.com/iffsid/mmvae> except for two differences. Firstly, the MNIST image is rescaled to a size of 32×32 to fit the DCGAN architecture. Secondly, the original training set is used to generate cross-validation folds using stratified 5-fold split. To generate pairs in each split, each instance of a digit class in one dataset is randomly paired with 20 instances of the same digit class from the other dataset.

I.2. Model Architecture

DCGAN (Radford et al., 2015) is used as the encoder in the natural image experiments. The DCGAN encoder includes 4 convolutional layers. The 4 convolutional layers have 32, 64, 128, 64 output units, and 16^2 , 8^2 , 4^2 , 1^2 output dimensions, respectively. The model is trained for 200 epochs using the RAdam optimizer with a batch size of 64 and a learning rate of 0.0004.

I.3. Results

We first train a UPLS model on each view of each dataset independently. We then train a PXL model on each two-view dataset, re-

Table I.1: **Within-sample inference performance.** UPLS and PXL show comparable within-sample inference performance. Interestingly, PXL is slightly better than UPLS on SVHN test set.

Training Set	Model	Rotated	Noisy
Two-view MNIST	UPLS	0.991 ± 0.000	0.989 ± 0.000
Two-view MNIST	PXL	0.987 ± 0.011	0.984 ± 0.009
Training Set	Model	MNIST	SVHN
MNIST-SVHN	UPLS	0.989 ± 0.001	0.860 ± 0.003
MNIST-SVHN	PXL	0.991 ± 0.001	0.868 ± 0.001

spectively. We repeat the experiments using 5-fold cross-validation.

As presented in Table I.1, both UPLS and PXL show comparable within-sample inference performance in general. UPLS performance is slightly better than PXL on two-view MNIST while PXL is better on MNIST-SVHN. Interestingly, we are able to achieve nearly perfect inference performance on MNIST regardless of learning paradigms, but the performance on SVHN is not ideal. One possibility can be that the SVHN image is an RGB image with three channels while the MNIST image is in grayscale with only one channel. Also note that the inference performance on SVHN improves from 0.860 in UPLS to 0.868 in PXL, suggesting PXL has the potential to achieve optimal result in a more challenging task.

From CKA result in Figure I.1, we observe that PXL improves between-view representational similarity on both datasets, empirically demonstrating the feasibility of PXL to capture invariant representations between different views in latent space. Thus we have shown that PXL can improve the representational similarity compared to UPLS on datasets paired by labels.

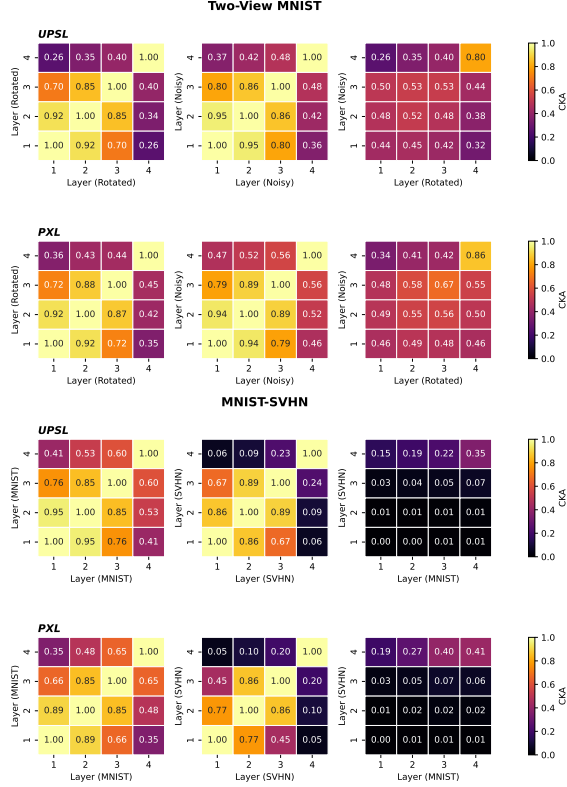


Figure I.1: CKA on natural images. The rows correspond to UPSL and PXL CKA on two-view MNIST dataset, and UPSL and PXL CKA on MNIST-SVHN dataset correspondingly. The left two columns represent within-view CKA while the right column shows between-view CKA.